PERGAMON

International Journal of Solids and Structures 40 (2003) 3853–3868

INTERNATIONAL JOURNAL OF SOLIDS and STRUCTURES

www.elsevier.com/locate/ijsolstr

Comparative analysis of extrinsic and intrinsic cohesive models of dynamic fracture

Dhirendra V. Kubair, Philippe H. Geubelle *

Department of Aeronautical and Astronautical Engineering, Center for the Simulation of Advanced Rockets, 306 Talbot Laboratory, University of Illinois at Urbana-Champaign, 104 South Wright Street, Urbana, IL 61801, USA

Received 1 November 2002; received in revised form 14 March 2003

Abstract

A comparative analysis of intrinsic and extrinsic cohesive models has been performed for the case of spontaneous and steady-state dynamic crack propagation. Spontaneous crack propagation was simulated using a spectral form of the elastodynamic boundary integral equation, while steady-state solutions were obtained by numerically integrating the governing Cauchy singular integral equation. Spontaneous crack propagation results showed that intrinsic models are less numerically stable than the extrinsic ones. Under steady-state propagation conditions, some intrinsic cohesive models lead to unrealistic results as the crack opening velocity becomes negative at the cohesive zone tip. By imposing a positive crack opening acceleration at the cohesive zone tip, the envelope of the required minimum initial strength has been calculated.

Keywords: Dynamic fracture; Crack; Propagation

1. Introduction

Since their introduction by Dugdale (1960) and Barenblatt (1962), cohesive zone models have been widely used in the theoretical and numerical treatment of quasi-static and dynamic fracture events. Cohesive zone models have recently been the object of a surge in interest, as they constitute the foundation of a new class of finite element schemes referred to as cohesive–volumetric finite element (CVFE) schemes developed especially for the simulation of fracture problems involving the spontaneous initiation, propagation and possible arrest of one or more cracks. As the CVFE denomination indicates, these schemes consist in a combination of conventional (volumetric) finite elements used to capture the mechanical response of the material, and interfacial (cohesive) elements used to model the progressive failure of the medium in the vicinity of the crack front.

* Corresponding author. Tel.: +1-217-244-7648; fax: +1-217-244-0720.
E-mail address: geubelle@uiuc.edu (P.H. Geubelle).

0020-7683/03/$ - see front matter © 2003 Elsevier Science Ltd. All rights reserved.
doi:10.1016/S0020-7683(03)00171-9

Two basic approaches have been proposed to implement cohesive failure models in the CVFE scheme. The first approach, referred to as the *intrinsic* method, characterizes the cohesive element response by a traction–separation curve that, starting from the origin, has a *hardening* (rising) portion that denotes an increasing resistance of the cohesive surface to separation. When sufficient separation is achieved, the cohesive traction reaches a maximum value corresponding to the failure strength τ^c of the material. The traction–separation curve then follows a *weakening* (decreasing) portion associated with the failure process. When the separation δ reaches a critical value δ^c, the cohesive traction τ is assumed to vanish, leading to the creation of a traction-free surface (i.e., a crack) in the discretised domain. The area under the traction–separation curve corresponds to the fracture toughness G^c of the material. This approach was first introduced within the context of the finite element method by Needleman (1987), who used a polynomial form for the traction-separation law in the modeling of void nucleation associated with particle debonding. Other cohesive models used in fracture simulations include exponential (Needleman, 1997), bilinear (Geubelle and Baylor, 1998) and trapezoidal (Tvergaard and Hutchinson, 1992) formulations.

The second approach, referred to as *extrinsic*, relies on the modeling of the failure (decreasing) portion of the cohesive law only. In other words, in this model, the cohesive traction is set equal to the material strength. Various models have been introduced to represent the damage dependence of cohesive strength. The initial model by Dugdale (1960) and Barenblatt (1962) assumed that the strength remains constant up to the critical value of the displacement jump δ^c. Yoshiaki and Aki (1972) introduced a damage-dependent cohesive law for which the strength decreases from its original value τ^c to zero. The most common model of that type is the linear model used extensively in a variety of dynamic fracture simulations based on the spectral scheme (Geubelle and Rice, 1995) and the CVFE scheme (Camacho and Ortiz, 1996). As was the case before, the area under the curve corresponds to the fracture toughness G^c of the material. This particular model is referred to as extrinsic because, unlike in the intrinsic case for which the damage initiation criterion is inherently contained in the model, this second approach requires the introduction of a separate criterion for the initiation of the failure process (i.e., for the introduction of cohesive elements in the CVFE scheme).

However, while both approaches are based on very similar concepts, the intrinsic and extrinsic models present some important differences, the effect of which is not completely understood. In a recent publication, Falk et al. (2001) have presented a comparative study of dynamic crack branching using intrinsic and extrinsic CVFE codes. They showed some important differences between the two methods. The objective of the present paper is somewhat different: it aims at shedding some light on the similarities and differences between these two cohesive zone models with regards to the fundamental problem of the steady-state and transient motion of a mode 3 crack propagating dynamically along its original plane in a linearly elastic medium. The analysis is performed in terms of the general cohesive model shown in Fig. 1, which combines the characteristics of both extrinsic and intrinsic cohesive models: like extrinsic models, it starts from a finite initial strength τ^i, but, as in the intrinsic case, it is not monotonic.

This study builds on the quasi-static results presented by Ungsuwarungsri and Knauss (1988a,b), who used the same model as that described in Fig. 1 and observed that only a limited strengthening is possible in order to obtain physically meaningful solutions to the cohesive variables. This issue is revisited here in the more general case of steady-state and transient crack propagation. The spectral scheme (Geubelle and Rice, 1995) is used in our spontaneous crack propagation simulations, while, under steady-state setting, the governing Cauchy singular equation relating the cohesive tractions and the slope of the displacement jumps is solved (Kubair et al., 2003). This paper is organized in the following manner: in Section 2, the mathematical description of the general cohesive model used in this study is presented, followed, in Section 3, by the results of the spectral scheme simulations of spontaneous dynamic crack motion. The last section summarizes the results of the steady-state analysis.

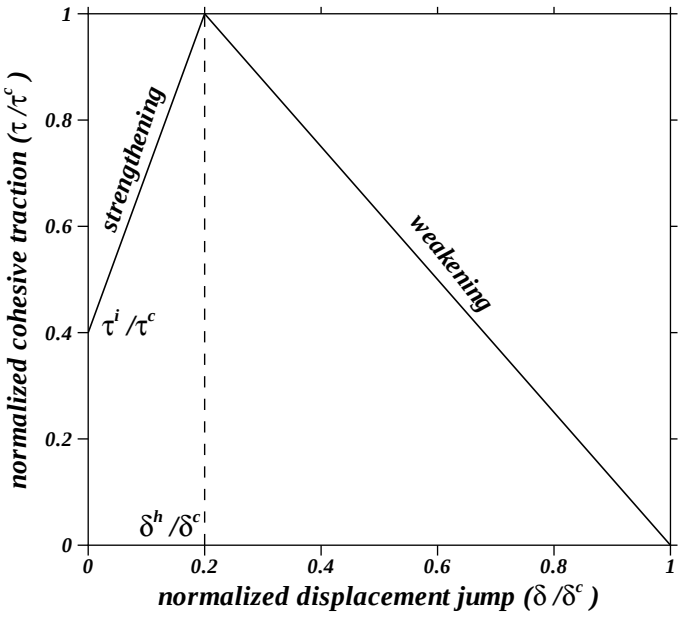

Fig. 1. General intrinsic cohesive zone model.

2. Cohesive zone model

As indicated above, the analysis summarized hereafter is performed in the simpler mode 3 case. It is important to note however that the conclusions relative to the intrinsic and extrinsic cohesive models drawn from the mode 3 analysis can be directly translated to the other pure modes of fracture (Kubair et al., 2003). The cohesive model described here is a combination of both intrinsic and extrinsic type laws and is depicted in Fig. 1.

Mathematically, the cohesive law can be written as

$$t = \left\langle \left[(1 - t^{\mathrm{i}}) \frac{d}{d^{\mathrm{h}}} + t^{\mathrm{i}} \right] \mathbf{H}(d^{\mathrm{h}} - d) + \left[\frac{1-d}{1-d^{\mathrm{h}}} \right] \mathbf{H}(d - d^{\mathrm{h}}) \right\rangle, \tag{1}$$

where $\langle \phi \rangle = \phi$ for $\phi > 0$ and zero otherwise, and $\mathbf{H}$ is the Heaviside function. In (1), t and t^{i} are defined in terms of the cohesive traction τ_3, the critical strength τ_3^{c} and the initial strength τ_3^{i} as

$$t = \frac{\tau_3}{\tau_3^{\mathrm{c}}}, \quad t^{\mathrm{i}} = \frac{\tau_3^{\mathrm{i}}}{\tau_3^{\mathrm{c}}}. \tag{2}$$

In the general case, the cohesive traction τ_3 is specified as an explicit function of the displacement jump δ_3. For these models referred to hereafter as *damage-dependent* models, d and d^{h} in Eq. (1) denote the normalized displacement jumps

$$d = \frac{\delta_3}{\delta_3^{\mathrm{c}}}, \quad d^{\mathrm{h}} = \frac{\delta_3^{\mathrm{h}}}{\delta_3^{\mathrm{c}}}, \tag{3}$$

where δ_3 is the crack opening displacement, δ_3^{c} is the critical crack opening displacement and δ_3^{h} is referred to as the hardening displacement, i.e., the displacement jump corresponding to the critical strength τ_3^{c}

(Fig. 1). When the initial strength is less than the critical strength ($t^{\mathrm{i}} < 1$), the cohesive model is intrinsic. When $t^{\mathrm{i}} = 1$ with $d^{\mathrm{h}} = 0$, it represents the extrinsic model. The area under the traction–separation curve represents the fracture toughness and has a simple closed-form expression when the model is damage dependent. However, only a numerical solution is possible for the cohesive zone variables δ_3 and τ_3 when the cohesive model is damage dependent, i.e., when d in (1) denotes the normalized displacement jump as in (3). A closed-form expression for the cohesive zone variables is however possible under steady-state propagation conditions when the cohesive traction τ_3 is no longer an explicit function of the displacement jump δ_3 but is expressed in terms of the cohesive zone coordinate x_1 and this simplified case, referred to hereafter as *spatially dependent* cohesive models.

In that case, the variables d and d^{h} entering (1) are defined by

$$d = \frac{x_1}{L_{\mathrm{c}_3}}, \quad d^{\mathrm{h}} = \frac{L_{\mathrm{h}}}{L_{\mathrm{c}_3}}, \tag{4}$$

where L_{c_3} is the cohesive zone length and L_{h} is the portion in the cohesive zone in which strengthening occurs and henceforth referred to as the *hardening length*, i.e, the spatial position corresponding to the critical strength τ_3^{c}. The spatially dependent and damage-dependent models have similar solution characteristics. Therefore, closed-form solutions obtained for the spatially dependent cohesive law provide valuable insight on the cohesive modeling of fracture.

3. Transient spontaneous crack propagation

A numerical technique recently developed for the analysis of fundamental dynamic fracture problems, the spectral scheme (Geubelle and Rice, 1995) is used here to simulate the spontaneous transient motion of a mode 3 crack. The spectral scheme is a special form of the elastodynamic boundary integral formulation and is best suited for the analysis of the failure process taking place in the vicinity of a spontaneously propagating planar crack embedded in an infinite, linearly elastic medium. It allows for the incorporation of a wide range of intrinsic and extrinsic cohesive failure models. The integral relation between the traction stresses acting on the fracture plane and the resulting displacement jump and its rate for a mode 3 crack was implemented by Morrissey and Geubelle (1997). The expression relating the traction on the fracture plane to the displacement jump and its rate is given by

$$\tau_3(x_1,t) = \tau_3^0(x_1,t) - \mu\frac{\dot{\delta}_3(x_1,t)}{c_{\mathrm{s}}} + f_3(x_1,t), \tag{5}$$

where τ_3 and δ_3 respectively denote the traction stress and displacement jump along the plane $x_2 = 0$, τ_3^0 corresponds to the externally applied stress that would be present on the fracture plane in the absence of the crack, μ is the shear modulus and $c_{\mathrm{s}} = \sqrt{\mu/\rho}$ is the shear wave speed with ρ being the density of the material. In the above equation, f_3 is the convolution term and is expressed in the Fourier domain as a convolution over the past displacement jump history as

$$\{\delta_3(x_1,t), f_3(x_1,t)\} = \{D_3(k,t), F_3(k,t)\}\mathrm{e}^{\mathrm{i}kx_1}, \tag{6}$$

with

$$F_3(k,t) = -\frac{\mu|k|}{2}\int_{-\infty}^{t} H_3(|k|c_{\mathrm{s}}t')D_3(k,t-t')|k|c_{\mathrm{s}}\,\mathrm{d}t', \tag{7}$$

where k is the spectral mode number. In (6) and (7), $F_3(k,t)$ and $D_3(k,t)$ are the time-dependent Fourier coefficients of the convolution term $f_3(x_1,t)$ and crack opening displacement $\delta_3(x_1,t)$, respectively. The convolution kernel H_3 for the mode 3 case is given by

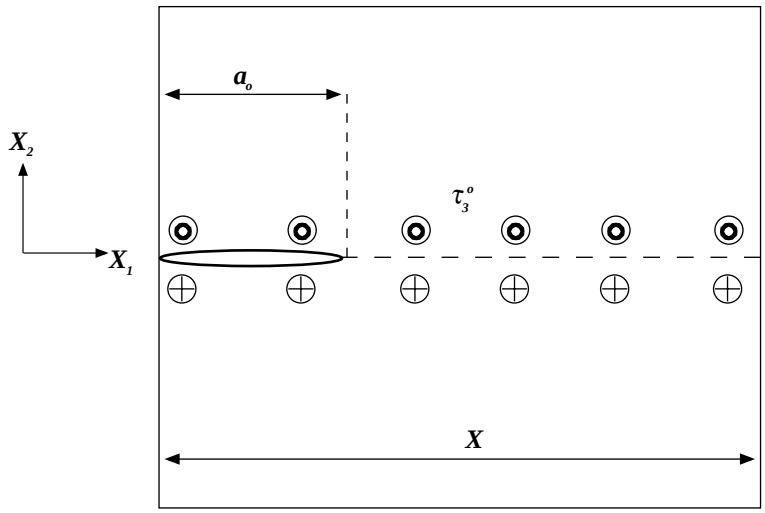

Fig. 2. Model dynamic fracture problem used in the spectral simulations.

$$H_3 = \frac{J_1(T)}{T}, \tag{8}$$

where J_1 is the Bessel function of the first kind. Similar relations have been derived for the other fracture modes (Geubelle and Rice, 1995). To simulate the spontaneous motion of the planar crack, the integro-differential relation (5) on the fracture plane needs to be supplemented with a cohesive failure model and in the present study, the general intrinsic damage-dependent cohesive law (1) is used.

To understand the effect of the various parameters entering the general cohesive law (1) on the transient motion of the mode 3 crack, the model fracture problem shown in Fig. 2 is solved. A 2-D planar crack of initial length a_0 subjected to uniform antiplane shear loading propagates spontaneously along the fracture plane. Crack growth is restricted to half of the domain length ($X/2$) to avoid the replication effects that arise due to the spectral representation (6) (Geubelle and Rice, 1995). The length X of the domain is set to $16a_0$. The accuracy of the spectral scheme depends on the number of terms chosen in the Fourier series representation of the solution. A convergence study was performed by varying the number of sampling points from 256 (2^8) to 8192 (2^{13}), and revealed that a minimum of 1024 (2^{10}) terms are required to obtain spatial convergence. This discretisation leads to a sampling point spacing $\Delta x = a_0/256$. The time step size $\Delta t = 0.2\Delta x/c_s$ is used to achieve a numerically stable solution. In our simulations, the shear modulus and the maximum strength are chosen to be $\mu = 10$ MPa and $\tau_3^c = 1$ MPa, respectively. The critical crack opening displacement δ_3^c ($a_0/55 \leqslant \delta_3^c \leqslant a_0/30$) and hardening displacement δ_3^h ($0.01\delta_3^c \leqslant \delta_3^h \leqslant \delta_3^c$) are varied in the present study.

Snapshots of the normalized crack opening profile δ_3 are shown in Fig. 3. The extent of the cohesive zone is indicated by the horizontal dotted lines $\delta_3/\delta_3^c = \pm 1$. These snapshots were recorded at constant time intervals of $c_s\Delta t/a_0 = 0.65$. As apparent in the figure, the separation distance between successive crack profiles is almost constant, indicating that the crack has reached a quasi-steady state propagation regime. The crack tip position of the respective snapshots corresponding to both the extrinsic and intrinsic models are almost at the same spatial position, which indicates that the propagation velocity of the crack is the same for these two models. Due to lack of cohesion at the cohesive zone tip in the intrinsic model, the entire crack plane separates by the initial displacement δ_3^i given by

$$\frac{\delta_3^i}{\delta_3^c} = \frac{\tau_3^0}{\tau_3^c}\frac{\delta_3^h}{\delta_3^c}. \tag{9}$$

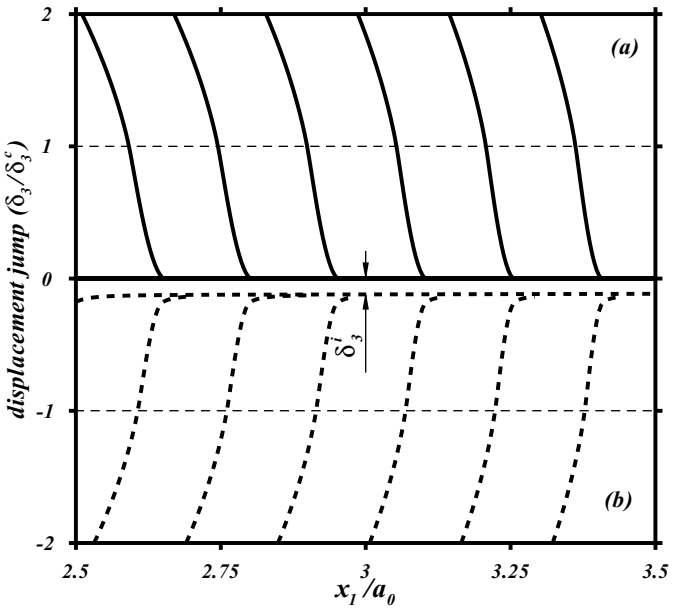

Fig. 3. Comparison of the crack profiles for extrinsic (case 'a') and intrinsic (case 'b') cohesive models. To avoid overlapping, the profiles for the intrinsic cohesive model are shown as negative. The profiles are for an external load of $\tau_3^0 = 0.6\tau_3^c$ and critical crack opening $\delta_3^c = 0.0267a_0$. The hardening displacement was chosen to be $\delta_3^h = 0.2\delta_3^c$ in the intrinsic model.

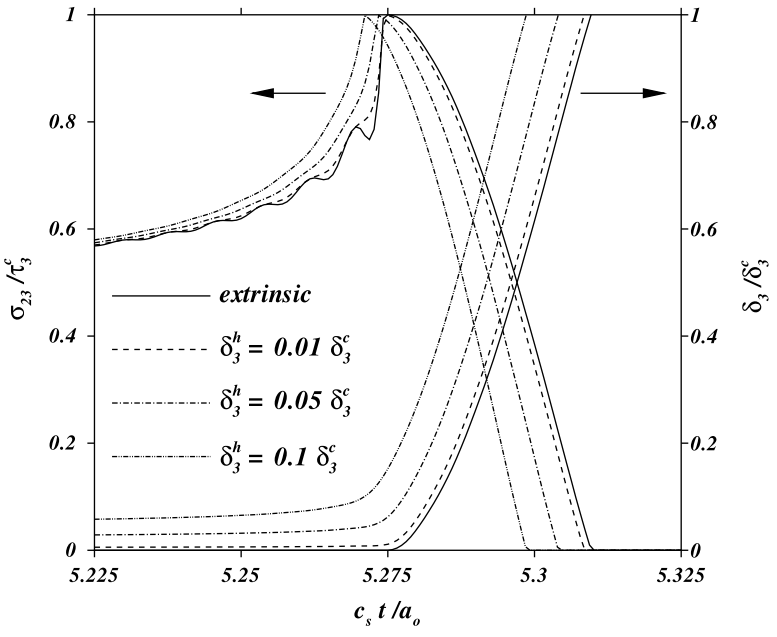

Fig. 4. Traction stress and opening displacement history at a point located at a distance $4.4a_0$ away from the initial right crack tip. The critical crack opening displacement is $\delta_3^c = 0.0267a_0$ and the crack is subjected to a loading of amplitude $\tau_3^0 = 0.5\tau_3^c$. The intrinsic models considered here have an initial strength $\tau_3^i = 0$. With decrease in the hardening displacement δ_3^h the curves for the displacement history tend towards the extrinsic model (solid curve).

As apparent in Fig. 3, the length of the cohesive zone is larger for the intrinsic model compared to that obtained for the extrinsic model and the crack opening profile is quite different.

The effect of varying the hardening displacement δ_3^h is illustrated in Fig. 4 by tracking the shear stress σ_{23} and opening displacement δ_3 at a point located at a distance $4.4a_0$ away from the initial right crack tip. The crack has reached a quasi-steady state of propagation when it has arrived at this point of observation. In the extrinsic case, the displacement remains zero until the crack reaches the observation point and the cohesive failure begins only once the cohesive zone tip reaches this point. Once the crack tip reaches the point of observation, the cohesive traction vanishes. With the intrinsic cohesive model, the scenario is quite different: at the instant the load is applied, the entire crack plane separates as the cohesive traction becomes equal to the applied loading. As mentioned earlier, the initial displacement increases with the hardening displacement (Eq. (9)). As the crack approaches the observed point, the crack opening displacement increases, which triggers the strengthening process. Once the cohesive tractions reaches the maximum (critical) strength, the weakening process begins. The opening velocity, which remained small during the strengthening phase, increases rapidly in the weakening portion. The opening velocity and the rate of decay of the cohesive tractions in the weakening portion increase with the hardening displacement, resulting in a reduction of the duration of the weakening process. The duration of the cohesive action in the intrinsic model includes both the hardening and weakening processes, as opposed to the exclusive weakening process in the extrinsic model. Since the crack has reached a quasi-steady state of propagation when it reaches the observation point, a longer duration of the cohesive failure process in the intrinsic model directly translates into a longer cohesive zone. This increase in the cohesive zone length is also illustrated by the crack profile snapshots shown in Fig. 3. With the decrease in the hardening displacement, the weakening portion for the intrinsic model tends towards the extrinsic model. Theoretically, when δ_3^h is zero, curves from both the extrinsic and intrinsic models will become coincident.

It is also worth noting however that, as the hardening displacement δ_3^h decreases, the numerical implementation of the intrinsic model becomes increasingly unstable. To investigate this issue of stability, a systematic error analysis has been performed to determine the maximum value of the time step size (characterized by the non-dimensional parameter $\beta = c_s\Delta t/\Delta x$) that provides a converged and stable solution. The simulations were performed with 2048 term in the Fourier series, and the intrinsic cohesive models had $\tau_3^i = 0$. The reference value of β was chosen as $\beta^R = 0.1$ since this value led to a time-converged solution for the entire range of the hardening displacement tested in this study ($0.01 \leqslant \delta_3^h/\delta_3^c \leqslant 0.05$). The error measure used to quantify numerical convergence was chosen as the relative difference (ε) on the time integral of the traction stress τ_3 recorded at a distance a_0 ahead of the initial crack tip:

$$\varepsilon = \frac{\int_0^T \tau_3(t)\,\mathrm{d}t}{\int_0^T \tau_3^R(t)\,\mathrm{d}t} - 1, \tag{10}$$

where $\tau_3^R(t)$ corresponds to the reference time history corresponding to $\beta^R = 0.1$ and the integration is performed from $t = 0$ until the end of the failure process ($t = T$) at the point of observation. The solution is said to be time converged when $\varepsilon < 1\%$. For higher values of the time step (Δt or β), numerical oscillations begin to affect the precision of the solution (as illustrated in Fig. 4) and may ultimately lead to the complete instability of the numerical scheme. The resulting stability map is presented in Fig. 5, in which the aforementioned effect of the hardening displacement on the stability of the numerical scheme is clearly visible. It is worth noting that the implementation of the extrinsic model achieves convergence for $\beta = 0.4$.

The crack profiles obtained for the general cohesive model with $\tau_3^i > 0$, are similar to those for the intrinsic case ($\tau_3^i = 0$) shown in Fig. 3. As expected, when the applied load is greater than the initial strength, the entire crack plane separates by δ_3^i before the actual cohesive process begins, while for loads less than the initial strength the initial displacement is zero. The initial displacement δ_3^i in terms of the external load, initial strength and hardening displacement is given by

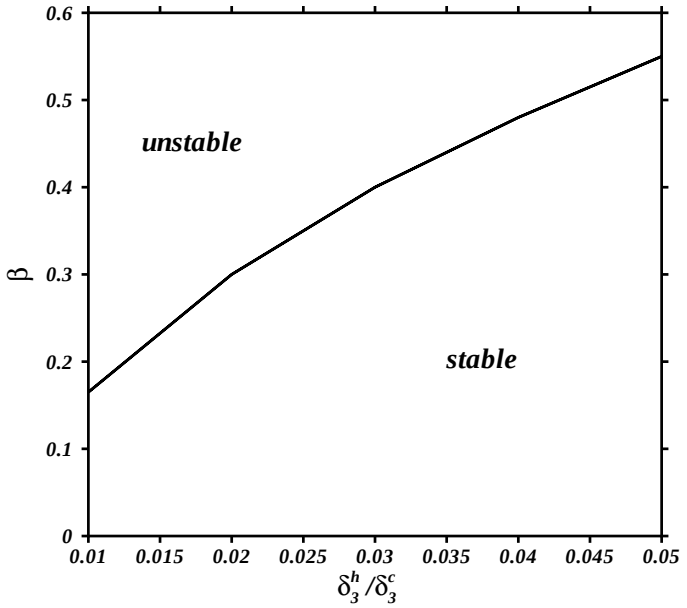

Fig. 5. Stability map illustrating the effect of the hardening parameter (δ_3^{h}) on the maximum allowable time step size. The fracture parameters used to obtained this map were $\delta_3^{\mathrm{c}} = 0.0267a_0$ and $\tau_3^0 = 0.5\tau_3^{\mathrm{c}}$.

$$\frac{\delta_3^{\mathrm{i}}}{\delta_3^{\mathrm{c}}} = \left\langle \frac{\tau_3^0 - \tau_3^{\mathrm{i}}}{\tau_3^{\mathrm{c}} - \tau_3^{\mathrm{i}}} \right\rangle \frac{\delta_3^{\mathrm{h}}}{\delta_3^{\mathrm{c}}}, \tag{11}$$

where $\langle\phi\rangle = \phi$ for $\phi > 0$ and zero otherwise.

The energetics involved in the failure process for a general cohesive model is depicted in Fig. 6, which presents the history of the rate of energy release defined as

$$\dot{E}_3 = \int \tau_3 \dot{\delta}_3 \, \mathrm{d}x, \tag{12}$$

where $\dot{\delta}_3$ is the crack opening velocity. The integration in Eq. (12) is performed over the cohesive length L_{c_3}, defined as the portion of the fracture plane for which $\delta_3^{\mathrm{i}} \leqslant \delta_3 \leqslant \delta_3^{\mathrm{c}}$, where δ_3^{i} is the initial displacement of the entire crack plane defined in Eq. (11). The rate of energy release is normalized by the fracture toughness G_3^{c} given by the area under the traction–separation curve

$$G_3^c = \frac{\tau_3^{\mathrm{c}}\delta_3^{\mathrm{c}}}{2}\left(1 + \frac{\tau_3^{\mathrm{i}}\delta_3^{\mathrm{h}}}{\tau_3^{\mathrm{c}}\delta_3^{\mathrm{c}}}\right). \tag{13}$$

Note that for any combinations of non-zero initial strength and hardening displacement, the fracture toughness for the intrinsic model is greater than the extrinsic model for the same critical strength (τ_3^{c}) and critical crack opening displacement (δ_3^{c}). The effect of applying a loading amplitude either greater or smaller than the initial strength is also illustrated in this figure. When the loading amplitude is less than the initial strength, the energy evolution for both the extrinsic and intrinsic models are similar. Note also the existence of a quasi-steady-state regime of propagation indicated by the quasi-constant value of the rate of energy release attained after the crack has grown by a sufficient distance. The above observation is the motivation for the steady-state analysis presented next.

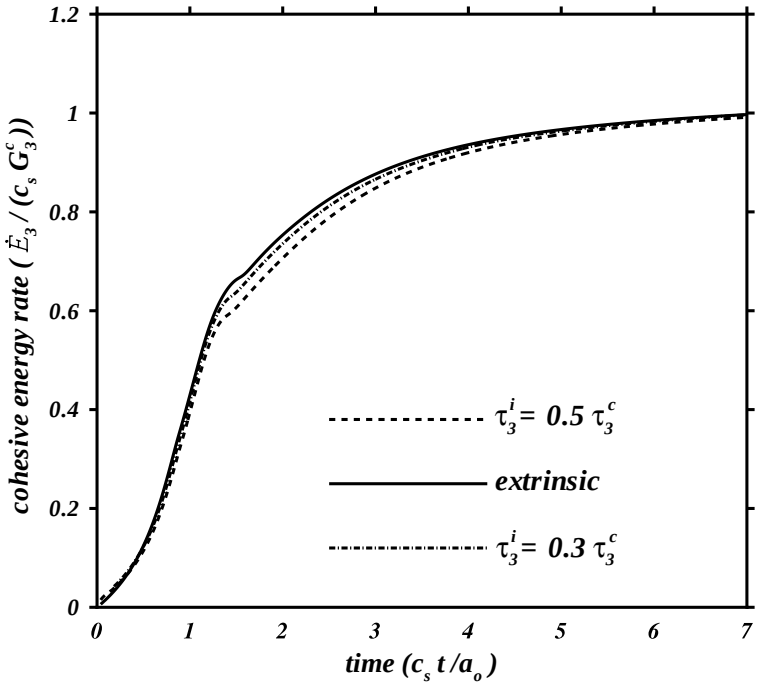

Fig. 6. Comparison of the energetics of the spontaneous crack propagation for the extrinsic and intrinsic models. The results shown here correspond to a hardening displacement $\delta_3^h = 0.1\delta_3^c$ and a loading amplitude $\tau_3^0 = 0.4\tau_3^c$.

4. Steady-state propagation

We now consider the basic problem of a semi-infinite crack propagating at a steady velocity v_c under anti-plane strain conditions in a linearly elastic solid. A moving Cartesian coordinates (x_1, x_2) is defined with its origin following the crack tip. The crack is subjected to an external crack plane loading τ_3^0 over the entire crack plane, as shown in Fig. 7. The material properties in this steady-state analysis are chosen to be the same as that in the spontaneous crack propagation simulations ($\tau_3^c = 1$ MPa, $\mu = 10$ MPa). Under steady-state propagation, the slope of the displacement jump is related to the cohesive tractions by the Cauchy singular integral equation (Kubair et al., 2003)

$$\delta_3'(x) = \frac{A_3}{\pi}\frac{\tau_3^c}{\mu}\int_0^1 \sqrt{\frac{x}{\eta}}\frac{t}{(x-\eta)}\,\mathrm{d}\eta, \tag{14}$$

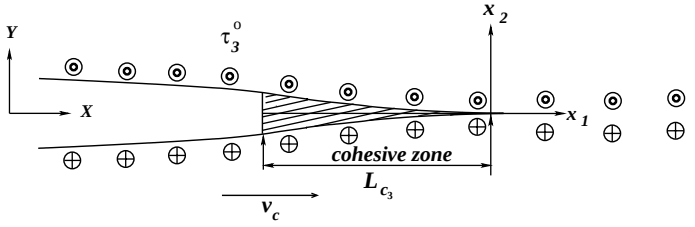

Fig. 7. Steady-state fracture problem.

where $\delta_3' = \mathrm{d}\delta_3/\mathrm{d}x$, t has been defined in (2), and

$$x = \frac{-x_1}{L_{c_3}}, \quad A_3 = \frac{4}{\sqrt{1-(v_c/c_s)^2}}. \tag{15}$$

L_{c_3} is the length of the cohesive zone, which is determined by satisfying the following condition at the cohesive zone tip:

$$\delta_3(x=1) = \delta_3^c, \tag{16}$$

where δ_3^c is the critical crack opening displacement. As mentioned earlier, a closed-form expression for δ_3' is possible only for a spatially dependent cohesive law. For some general damage-dependent cohesive law, a numerical quadrature of the governing Cauchy singular equation is required to obtain a solution. Details of the numerical quadrature and Picard's iteration schemes can be found in the paper by Kubair et al. (2003).

The damage-dependent intrinsic model introduced in Section 2 has been analyzed under steady-state conditions and our results show that physically meaningful results are possible only for a range of non-zero values of the initial strength τ_3^i. Similar observation have been made by Ungsuwarungsri and Knauss (1988b) in their analysis of equilibrium crazes: they concluded that only limited strengthening was possible under steady-state propagation. However, our spectral simulations did not exhibit any numerical difficulty in the solution procedure. In order to illustrate the non-existence of a physically meaningful solution for a range of initial strengths τ_3^i, a closed-form expression for δ_3' using the spatially dependent cohesive model described by Eqs. (1), (2), (4) has been obtained:

$$\begin{aligned}\frac{\pi\mu}{A_3\tau_3^c}\delta_3'(\zeta) = {} & 2\left(1-\frac{\tau_3^i}{\tau_3^c}\right)\left\{\sqrt{\frac{\zeta}{L_h}}\tanh^{-1}\left[\sqrt{\frac{L_h}{\zeta}}\right]-1\right\}\sqrt{\frac{\zeta}{L_h}} + 2\frac{\tau_3^i}{\tau_3^c}\tanh^{-1}\left[\sqrt{\frac{L_h}{\zeta}}\right] \\ & + 2\frac{(1-\sqrt{L_h/L_{c_3}})}{1-L_h/L_{c_3}}\sqrt{\frac{\zeta}{L_{c_3}}} + \frac{2}{1-L_h/L_{c_3}}\left(1-\frac{\zeta}{L_{c_3}}\right)\left(\tanh^{-1}\left[\sqrt{\frac{L_{c_3}}{\zeta}}\right]-\tanh^{-1}\left[\sqrt{\frac{L_h}{\zeta}}\right]\right),\end{aligned} \tag{17}$$

where $\zeta = -x_1 \geqslant 0$. This solution for the spatially dependent cohesive law is similar to that obtained with the damage-dependent cohesive law and will be illustrated later with the results. The closed-form solution (17) for the spatially dependent model shows that a physically meaningful solution for δ_3' is possible only for a range of initial strengths τ_3^i. Indeed, an analysis of the closed-form expression for δ_3' (Eq. (17)) reveals that, when $\tau_3^i = 0$, the second slope of the displacement (δ_3''), which is analogous to crack opening acceleration ($\ddot{\delta}_3$), becomes negative at the cohesive tip. The negative opening acceleration leads to a negative energy ($\tau_3\delta_3' < 0$), violating the second law of thermodynamics and hence physically unacceptable (Costanzo and Allen, 1995). Under mode 1 loading, a negative crack opening acceleration and velocity lead to interpenetration of the crack faces, which is again physically unrealistic. A closed-form expression relating the minimum initial strength required $\tau_{3_{\min}}^i$ and the hardening length L_h was obtained by imposing a zero value for the crack opening curvature at the cohesive zone tip:

$$\lim_{x_1\to 0}[\sqrt{x_1}\delta''] = 0 \Rightarrow \tau_{3_{\min}}^i = \frac{\tau_3^c}{1+\sqrt{L_h/L_{c_3}}} \quad \forall L_h \in (0, L_{c_3}). \tag{18}$$

For the damage-dependent model, a closed-form expression for the required minimum initial strength is not possible. However we found the following expression

$$\tau_{3_{\min}}^i \approx \frac{\tau_3^c}{1+\beta\sqrt{\delta_3^h/\delta_3^c}}, \tag{19}$$

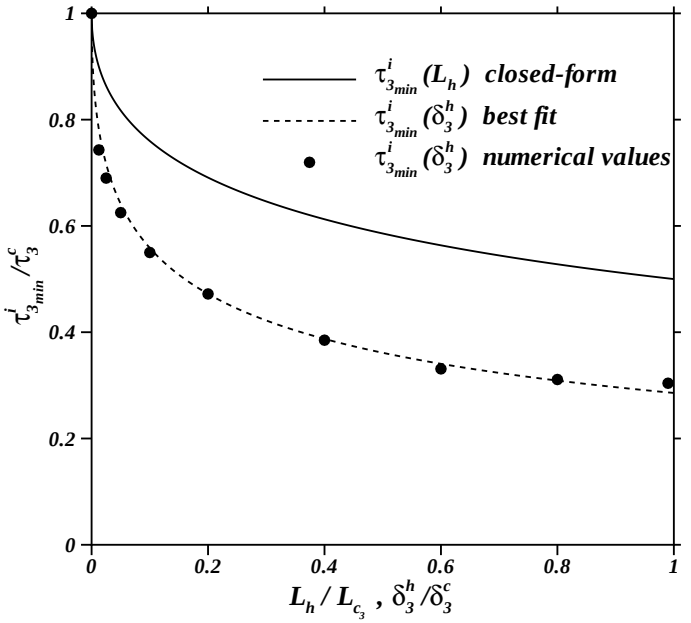

Fig. 8. Minimum initial strength required to obtain a physically meaningful steady-state solution as a function the hardening distance L_{h} (for the spatially dependent model) and the hardening displacement δ_3^{h} (for the damage-dependent model). The functional form of $\tau^{\mathrm{i}}_{3_{\mathrm{min}}}$ is given by Eqs. (18) and (19).

to fit the numerical values quite well with $\beta = 2.5$. The minimum initial strength required ($\tau^{\mathrm{i}}_{3_{\mathrm{min}}}$) as a function of the hardening length (L_{h}) and hardening displacement (δ_3^{h}) is shown in Fig. 8. A similar study using the trapezoidal cohesive model analogous to that used by Tvergaard and Hutchinson (1992) is summarized in Appendix A. To conclude this discussion of the minimum value of the initial strength, it is interesting to note that the existence of a similar negative opening velocity has also been observed by Marder and Gross (1995) in their quasi-steady state 1-D and 2-D molecular dynamics simulations of fracture instabilities with a quite different fracture model.

The length L_{c_3} of the cohesive zone can be determined by satisfying the following condition:

$$\frac{\pi}{A_3}\frac{\tau_3^0}{\tau_3^{\mathrm{c}}}\sqrt{\frac{\delta_3^{\mathrm{c}}}{L_{\mathrm{c}_3}}} = \int_0^1 \frac{t}{\sqrt{\eta}}\,\mathrm{d}\eta = \frac{4}{3}\left\{\frac{\tau_3^{\mathrm{i}}}{\tau_3^{\mathrm{c}}}\sqrt{\frac{L_{\mathrm{h}}}{L_{\mathrm{c}_3}}} + \frac{1}{1+\sqrt{L_{\mathrm{h}}/L_{\mathrm{c}_3}}}\right\}, \tag{20}$$

for the spatially dependent cohesive model. From the above expression, we can see that the amplitude of the externally applied load is always less than the initial strength τ_3^{i} under steady-state propagation conditions. Similar conclusions about the loading amplitude in the damage-dependent model can be reached due to the similarity between the spatially dependent and damage-dependent models.

As seen from the spectral scheme simulations, the entire crack plane separates by an amount δ_3^{i} (Eqs. (9) and (11)), when the initial strength is zero or when the applied load is greater than the initial strength. Steady-state solution with a prescribed initial displacement is possible by superposing a constant opening displacement, as it does not alter the governing Cauchy singular equation (14). However, our steady-state analysis showed that only initial displacements corresponding to an initial strength $\tau_3^{\mathrm{i}} \geqslant \tau^{\mathrm{i}}_{3_{\mathrm{min}}}$ converge to a physically meaningful solution and the relation between the initial displacement and initial strength is given by

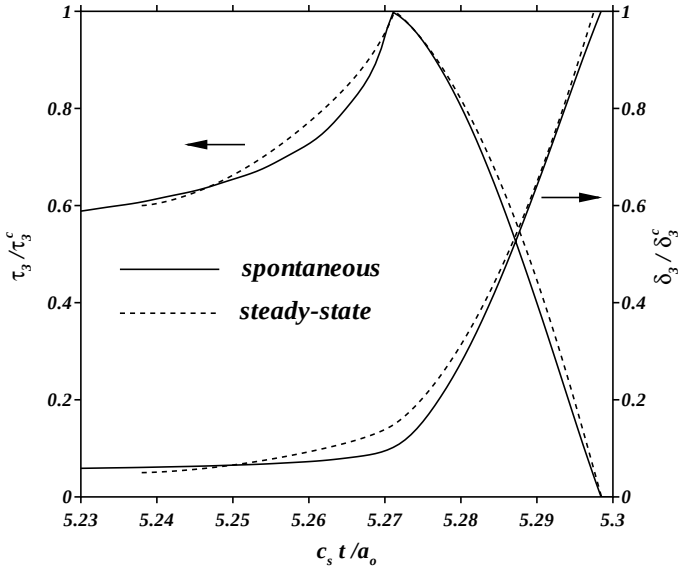

Fig. 9. Comparison of the steady-state results with the point history from the spectral simulations. The spectral results were obtained for $\tau_3^0 = 0.5\tau_3^c$, $\delta_3^c = 0.0267a_0$ and $\delta_3^h = 0.1\delta_3^c$ with a zero initial strength which resulted in a initial displacement $\delta_3^i = 0.05\delta_3^c$. A constant initial displacement jump was superposed on the steady-state solution for δ_3 which led to an initial strength of $\tau_3^i = 0.6\tau_3^c$. The spatial coordinates of the steady-state solution have been transformed into time for the sake of comparison ($v_c = 0.92c_s$).

$$\frac{\delta_3^i}{\delta_3^c} = \left(\frac{\tau_3^i}{\tau_3^c - \tau_3^i}\right)\frac{\delta_3^h}{\delta_3^c}. \tag{21}$$

In order to compare results from the spectral scheme with those obtained in the steady-state case, the point history of the cohesive traction τ_3 and crack opening displacement δ_3 have been tracked at a point sufficiently far away from the initial crack tip position ($4.4a_0$), where quasi-steady-state of propagation prevailed in our simulations (Fig. 9). The spatial coordinates of the steady-state solution have been transformed into time for the sake of comparison and the two solutions are in good agreement.

The spatial distribution of the slope of the crack sliding displacement in the cohesive zone is shown in Fig. 10. As mentioned earlier, under steady-state propagation conditions, δ_3' is equivalent to the crack sliding velocity $\dot{\delta}_3$. In the intrinsic model, the discontinuity in the slope of the cohesive traction/separation curve results in an inflection point in the spatial variation of δ_3' at $x_1 = L_h$. However, the variation of δ_3' in the weakening portion of the cohesive zone is similar to that for the extrinsic model and can be attributed to the same damage mechanism taking place in both models.

The normalized crack opening profiles for both the extrinsic and intrinsic models are shown in Fig. 11. In order to compare the crack opening profiles obtained from the spectral simulations, the initial strength and hardening displacements are chosen to be the same as those in the results shown in Fig. 3. The cohesive zone is longer in case of the intrinsic model as indicated by the smaller amplitude of the opening displacement at the cohesive zone tip (δ_3^c/L_{c_3}) for the intrinsic model. As seen from the spectral results (Fig. 3), the crack opening profiles in the intrinsic model has two distinct variations in the cohesive zone, one below and another above the hardening displacement δ_3^h. The variation of the crack opening displacement in the weakening region is similar to that obtained with the extrinsic model.

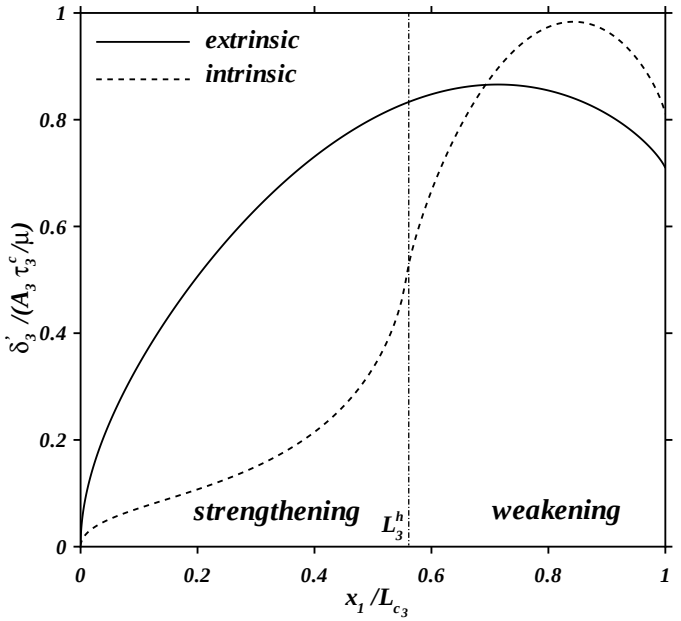

Fig. 10. Slope of the displacement jump for the extrinsic and intrinsic cohesive models. For the damage-dependent model, $\tau_3^i = 0.6\tau_3^c$ and $\delta_3^h = 0.2\delta_3^c$.

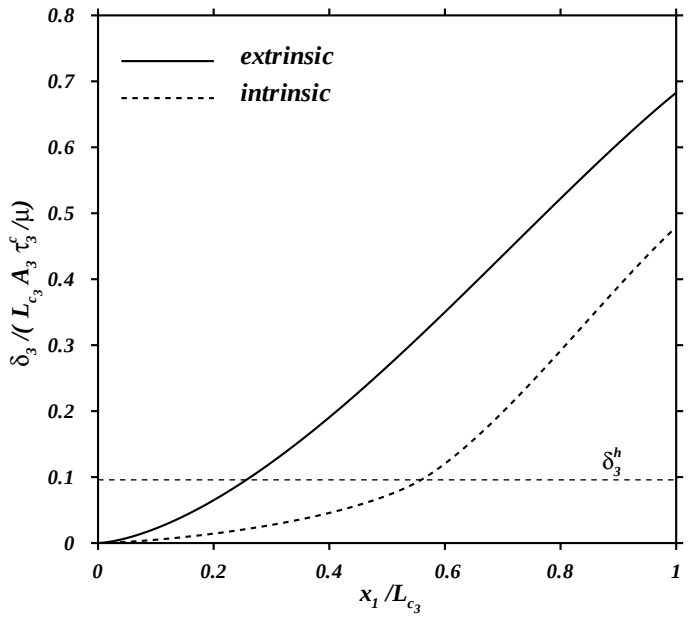

Fig. 11. Crack sliding profile in the cohesive zone for the extrinsic and intrinsic cohesive models. The fracture parameters in this figure are identical to those in Fig. 10. The opening profiles are similar to those obtained by the spectral scheme shown in Fig. 3.

5. Conclusions

A comparative analysis of extrinsic and intrinsic cohesive models has been performed under both spontaneous and steady-state dynamic crack propagation conditions. The results of the spontaneous simulations indicate that the implementation of intrinsic models is less numerically stable than that of the extrinsic models. The propagation velocity and energetics of the crack obtained with the intrinsic and extrinsic models are similar but details of the cohesive zone, namely the cohesive zone length and the crack opening profile, are somewhat different.

Under steady-state propagation conditions, a vanishing initial strength at the cohesive zone tip leads to a negative crack opening acceleration, which in turn leads to negative crack opening slope, leading to a physically unacceptable solution. By imposing a positive crack opening acceleration at the cohesive zone tip, the envelope of the minimum initial strength required was calculated in terms of the hardening displacement (or length).

Acknowledgement

Part of this work has been supported by the ASCI Center for the Simulation of Advanced Rockets funded by the U.S. Department of Energy through the University of California under subcontract number B341494.

Appendix A. Cohesive model with dwell portion

We obtain here the steady-state solution for the more general intrinsic cohesive model shown in Fig. 12 and expressed by

$$t = \left\langle \left[(1 - t^{\mathrm{i}}) \frac{d}{d^{\mathrm{h}}} + t^{\mathrm{i}} \right] \mathbf{H}(d^{\mathrm{h}} - d) + \mathbf{H}(d - d^{\mathrm{h}}) + \left[\frac{1 - d}{1 - d^{\mathrm{d}}} - 1 \right] \mathbf{H}(d - d^{\mathrm{d}}) \right\rangle, \tag{A.1}$$

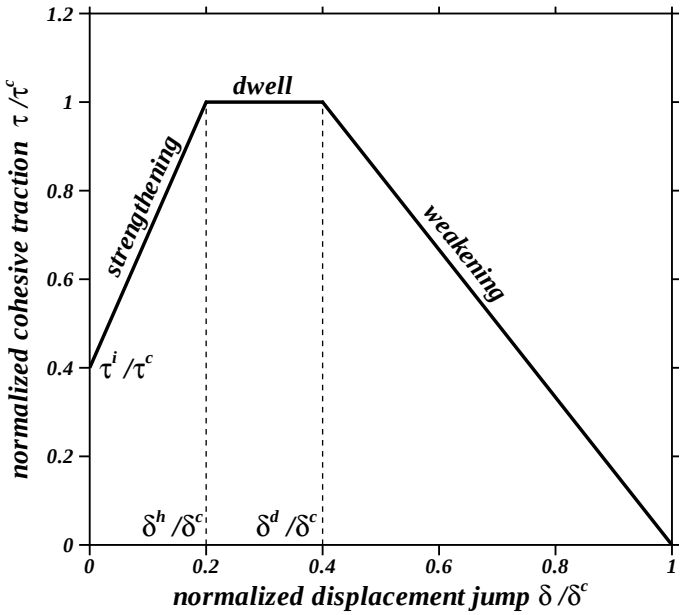

Fig. 12. Intrinsic cohesive law similar to the trapezoidal model introduced by Tvergaard and Hutchinson (1992).

where d^{d} is the dwell distance which is defined as $d^{\mathrm{d}} = L_{\mathrm{d}}/L_{\mathrm{c}_3}$ for a spatially dependent model and $d^{\mathrm{d}} = \delta_3^{\mathrm{d}}/\delta_3^{\mathrm{c}}$ for a damage-dependent model, with δ_3^{d} being the dwell displacement. When $d^{\mathrm{h}} = d^{\mathrm{d}}$, (A.1) reverts to (1) and, when $t^{\mathrm{i}} = 0$, (A.1) recovers the Tvergaard and Hutchinson (1992) trapezoidal cohesive model in the damage-dependent case. Closed-form expression for the slope of the displacement jump is possible for the spatially dependent model, and is given by

$$\begin{aligned}\frac{\pi\mu}{A_3\tau_3^{\mathrm{c}}}\delta_3'(\zeta) = {} & 2\left(1-\frac{\tau_3^{\mathrm{i}}}{\tau_3^{\mathrm{c}}}\right)\left\{\sqrt{\frac{\zeta}{L_{\mathrm{h}}}}\tanh^{-1}\left[\sqrt{\frac{L_{\mathrm{h}}}{\zeta}}\right]-1\right\}\sqrt{\frac{\zeta}{L_{\mathrm{h}}}}+2\frac{(1-\sqrt{L_{\mathrm{d}}/L_{\mathrm{c}_3}})}{1-L_{\mathrm{d}}/L_{\mathrm{c}_3}}\sqrt{\frac{\zeta}{L_{\mathrm{c}_3}}}\\ & +2\frac{\tau_3^{\mathrm{i}}}{\tau_3^{\mathrm{c}}}\tanh^{-1}\left[\sqrt{\frac{L_{\mathrm{h}}}{\zeta}}\right]+2\tanh^{-1}\left[\sqrt{\frac{L_{\mathrm{d}}}{\zeta}}\right]-2\tanh^{-1}\left[\sqrt{\frac{L_{\mathrm{h}}}{\zeta}}\right]\\ & +\frac{2}{1-L_{\mathrm{d}}/L_{\mathrm{c}_3}}\left(1-\frac{\zeta}{L_{\mathrm{c}_3}}\right)\left(\tanh^{-1}\left[\sqrt{\frac{L_{\mathrm{c}_3}}{\zeta}}\right]-\tanh^{-1}\left[\sqrt{\frac{L_{\mathrm{d}}}{\zeta}}\right]\right),\end{aligned} \tag{A.2}$$

where $\zeta = -x_1 \geqslant 0$. As expected, when the hardening length and the dwell length are the same, the above equation recovers Eq. (17).

The minimum initial strength required to obtain physically meaningful results under steady-state propagation conditions is found by limiting $\sqrt{x_1}\delta_3''(x_1 \to 0) = 0$ and is given by

$$\frac{\tau_{3_{\min}}^{\mathrm{i}}}{\tau_3^{\mathrm{c}}} = 1-\frac{1}{2}\sqrt{\frac{L_{\mathrm{h}}}{L_{\mathrm{d}}}}-\frac{(1-\sqrt{L_{\mathrm{d}}/L_{\mathrm{c}_3}})\sqrt{L_{\mathrm{h}}/L_{\mathrm{c}_3}}-(1-\sqrt{L_{\mathrm{h}}/L_{\mathrm{c}_3}})}{2(1-L_{\mathrm{h}}/L_{\mathrm{c}_3})}. \tag{A.3}$$

Note that this minimum initial strength is greater than the minimum initial strength given by Eq. (18) when $d^{\mathrm{d}} > d^{\mathrm{h}}$.

References

Barenblatt, G.I., 1962. The mathematical theory of equilibrium cracks in brittle fracture. Advances of Applied Mechanics 7, 55–129.

Camacho, G.T., Ortiz, M., 1996. Computational modeling of impact damage in brittle materials. International Journal of Solids and Structures 33, 2899–2938.

Costanzo, F., Allen, D.H., 1995. A continuum thermodynamic analysis of cohesive zone models. International Journal of Engineering Science 33 (15), 2197–2219.

Dugdale, D.C., 1960. Yielding of steel sheets containing slits. Journal of the Mechanics and Physics of Solids 8, 100–104.

Falk, M.L., Needleman, A., Rice, J.R., 2001. A critical evaluation of dynamic fracture simulations using cohesive surfaces. Journal de Physique IV 11, 43–52.

Geubelle, P.H., Rice, J.R., 1995. A spectral method for 3D elastodynamic fracture problems. Journal of the Mechanics and Physics of Solids 43, 1791–1824.

Geubelle, P.H., Baylor, J., 1998. Impact-induced delamination of laminated composites: a 2D simulation. Composites B 29, 589–602.

Kubair, D.V., Geubelle, P.H., Huang, Y.Y., 2003. Analysis of a rate-dependent cohesive model under dynamic crack propagation. Engineering Fracture Mechanics 50 (5), 685–704.

Marder, M., Gross, S., 1995. Origin of crack tip instabilities. Journal of the Mechanics and Physics of Solids 43, 1–48.

Morrissey, J.W., Geubelle, P.H., 1997. A numerical scheme for mode III dynamic fracture problems. International Journal of Numerical Methods in Engineering 40, 1181–1196.

Needleman, A., 1987. A continuum model for void nucleation by inclusion debonding. Journal of Applied Mechanics: Transactions of the ASME 54, 525–531.

Needleman, A., 1997. Numerical modeling of crack growth under dynamic loading conditions. Computational mechanics 19 (6), 463–469.

Tvergaard, V., Hutchinson, J.W., 1992. The relation between crack growth resistance and fracture process parameters in elastic–plastic solids. Journal of the Mechanics and Physics of Solids 40, 1377–1397.

Ungsuwarungsri, T., Knauss, W.G., 1988a. A nonlinear analysis of an equilibrium craze: Part I-Problem formulation and solution. Journal of Applied Mechanics: Transactions of the ASME 55, 44–51.

Ungsuwarungsri, T., Knauss, W.G., 1988b. A nonlinear analysis of an equilibrium craze: Part II-Simulations of craze and crack growth. Journal of Applied Mechanics: Transactions of the ASME 55, 52–58.

Yoshiaki, I., Aki, K., 1972. Seismic time function of propagating longitudinal-shear cracks. Journal of Geophysical Research 77 (11), 2034–2044.